PHYSICS OF FLUIDS **26**, 074103 (2014)

The structure of primary instability modes in the steady wake and separation bubble of a square cylinder

X. Mao[1,2,a] and H. M. Blackburn[1]
[1]*Department of Mechanical and Aerospace Engineering, Monash University, 3800, Melbourne, Australia*
[2]*School of Engineering and Computing Sciences, Durham University, Durham DH1 5AE, United Kingdom*

(Received 24 February 2014; accepted 25 June 2014; published online 15 July 2014)

Flows past symmetric two-dimensional bluff bodies such as the circular cylinder, the square cylinder, and the normal flat plate produce large separation bubbles which (in the steady restriction) may become very elongated at comparatively low Reynolds numbers. The present work focuses on the steady/symmetric wake of a square cylinder at $Re \leq 300$, which loses stability to anti-symmetric two-dimensional global modes at $Re_c = 45$. It is observed that while there is a continuous evolution in the parameters of the leading instability mode with increasing Re, a change in spatial structure of the modes begins near $Re = 175$, where the peak growth rate is found. At lower Re, instability modes are generally associated with the wake downstream of the separation bubble, but as Re increases the origin of the modes migrates into the separated shear layers. At the optimal Reynolds number $Re = 175$, the base flow streamlines around the end of the bubble are most parallel. The observed relation between structures of the bubble and global instabilities is explained on the basis of local stability analyses.
 [http://dx.doi.org/10.1063/1.4887518]

I. INTRODUCTION

The initial progression of primary and secondary instabilities of the wakes of symmetric bluff bodies with Reynolds number has received extensive study and is now moderately well understood:[1–3] the primary two-dimensional instability breaks the symmetry of the steady wake to produce periodic vortex shedding and the first two leading secondary three-dimensional instabilities break the space-time symmetry of the two-dimensional vortex street in the two generically possible ways.[4,5] The wake dynamics for Reynolds numbers much above a few hundred become chaotic and for a range of higher Reynolds number it becomes difficult to establish a simple understanding of wake processes. However, at still higher Reynolds numbers, the next clearly identifiable progression is that the separated shear layers themselves become unstable before they are engulfed into the turbulent wake, starting at $Re \sim 1000$.[1] Eventually with increasing Reynolds number these instabilities progress upstream to reach the separation points, bringing on the drag crisis for flow past a circular cylinder.

In the present work we study the two-dimensional global instability of the symmetric wake of a square cylinder: the wake is constrained to be symmetric (and consequently, at the Reynolds numbers studied, also steady) by imposing suitable boundary conditions on the wake centreline. As a result, the primary instability of the whole wake is of symmetry-breaking nature. However, as the separation bubble becomes more and more extended with increasing Reynolds number, the instability mode evolves from downstream of the separation bubble into the separated shear layers. Thus we are able to produce shear layer instabilities, reported to be related with two-dimensional Kelvin–Helmholtz instabilities in the near wake of the nonlinear saturated (vortex shedding) flow,[6] at relatively small

[a]Electronic mail: xuerui.mao@durham.ac.uk

Reynolds number, $Re \leq 300$, without progressing through three-dimensional regimes. Since we are here concerned with instability of the steady two-dimensional flow, the three-dimensional instability of the vortex shedding state, occurring at, e.g., $Re \geq 190$ for circular cylinder flow, is not considered in this work.

II. METHODOLOGY

In global stability analyses of flow past a square cylinder, we choose to place the origin of the Cartesian coordinate system at the centre of the square, with the x-axis aligned with the oncoming flow direction and the y-axis along the vertical direction. Taking the free stream flow speed U_∞ as a velocity scale and the side length of the square d as a length scale, fluid motion in primitive (velocity, pressure) variables can be described using the non-dimensional incompressible Navier–Stokes (NS) equations in a computational domain Ω:

$$\begin{aligned} \partial_t \boldsymbol{u} &= -\boldsymbol{u}\cdot\boldsymbol{\nabla}\boldsymbol{u} - \boldsymbol{\nabla} p + Re^{-1}\nabla^2\boldsymbol{u}, \\ \text{with} \quad \boldsymbol{\nabla}\cdot\boldsymbol{u} &= 0 \quad \text{in} \quad \Omega, \end{aligned} \tag{1}$$

where $\boldsymbol{u}$ is the velocity vector field and p is the modified pressure. The Reynolds number $Re = U_\infty d/\nu$. The flow field can be decomposed into the summation of a (steady) base flow field and a perturbation field as

$$(\boldsymbol{u}, p) = (\boldsymbol{U}, P) + (\boldsymbol{u}', p'). \tag{2}$$

The x-components of the base flow and perturbation will be denoted as U and u' while the y-components will be represented as V and v' when required in the following.

Substituting (2) into (1) and omitting interactions of the perturbation with itself, we obtain the linearized Navier–Stokes (LNS) equations:

$$\partial_t \boldsymbol{u}' = -\boldsymbol{U}\cdot\boldsymbol{\nabla}\boldsymbol{u}' - \boldsymbol{u}'\cdot\boldsymbol{\nabla}\boldsymbol{U} - \boldsymbol{\nabla} p' + Re^{-1}\nabla^2\boldsymbol{u}', \quad \text{with} \quad \boldsymbol{\nabla}\cdot\boldsymbol{u}' = 0. \tag{3}$$

This set of equations defines a linear evolution operator $\mathcal{A}$, which evolves perturbations forward in time:

$$\partial_t \boldsymbol{u}'(t) = \mathcal{A}(\boldsymbol{U})\boldsymbol{u}'(t).$$

The perturbation flow $\boldsymbol{u}'(t)$ can be decomposed as a linear summation of eigenmodes, $\boldsymbol{u}'(t) = \sum_{j=0}^{\infty} \hat{\boldsymbol{u}}_j \exp(\sigma_j t)$, where $\hat{\boldsymbol{u}}_j$ and σ_j are the eigenvectors and eigenvalues of the time-independent operator $\mathcal{A}$. It is noted that the real and imaginary parts of σ_j are the growth rate and frequency of the corresponding eigenvector or eigenmode $\hat{\boldsymbol{u}}_j$. The eigenmode with the largest growth rate is defined as the most unstable mode. Therefore if at least one of the eigenvalues of $\mathcal{A}$ has a positive real part, the corresponding eigenmode will grow in time and consequently the flow is unstable. When all the eigenvalues of $\mathcal{A}$ have negative real parts, the flow is asymptotically stable. To calculate the eigenvalues and eigenvectors of $\mathcal{A}$, we define an operator $\mathcal{M}$ evolving the perturbation from time $t = 0$ to $t = \tau$,

$$\boldsymbol{u}'(\tau) = \mathcal{M}(\tau)\boldsymbol{u}'(0).$$

It follows that $\mathcal{M}(\tau) = \exp(\tau\mathcal{A})$. Then an eigenvalue of $\mathcal{A}$ can be calculated as $\sigma = \tau^{-1}\ln\lambda$, where λ is an eigenvalue of $\mathcal{M}$ and the corresponding eigenvector is the eigenvector of $\mathcal{A}$ associated with eigenvalue σ.

To compute λ, the LNS equations are integrated iteratively to build a (Krylov) vector sequence: $\boldsymbol{u}'(0), \mathcal{M}\boldsymbol{u}'(0), \mathcal{M}^2\boldsymbol{u}'(0), \ldots, \mathcal{M}^N\boldsymbol{u}'(0)$, where $\boldsymbol{u}'(0)$ is a random initial perturbation and the leading eigenvalues and eigenvectors of $\mathcal{M}$ can be extracted from this sequence by an Arnoldi method.[7]

Where local stability analysis results are presented (Sec. VI), these were computed using sectional profiles of streamwise velocity component extracted from the base flows on a Chebyshev-spaced grid.[8] The method was cross-checked against the global stability code described above, using the same profiles in two-dimensional periodic domains of appropriate lengths.

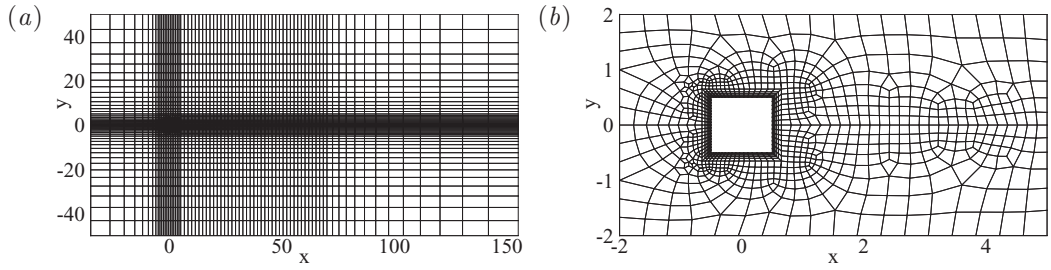

FIG. 1. Spectral element decomposition of the computational domain for direct numerical simulations (DNS) and stability analyses. (a) Whole domain; (b) subdomain close to the square.

III. DISCRETIZATION AND CONVERGENCE

Spectral elements employing piecewise continuous nodal-based tensor-product polynomial expansions with order P within mapped-quadrilateral elemental subdomains were adopted for spatial discretization,[9] as depicted in Fig. 1. A second-order-time scheme was chosen for the temporal discretization and the time step was set to $\Delta t = 2.5 \times 10^{-3}$. When solving the NS equations to obtain the base flows, the inflow and far-field boundary conditions are set to $\boldsymbol{U} = (1, 0)$ and zero Neumann and zero Dirichlet velocity boundary conditions are implemented on the outflow boundary and the surface of the square, respectively. When solving the LNS equations, zero Neumann conditions are used for velocity on the outflow boundary and zero Dirichlet is adopted for all the other boundaries.

Table I shows dependence of the eigenvalue of $\mathcal{A}$ with the largest real part, denoted as $\sigma_{\max}$, with respect to the spectral element polynomial order P. The eigenvalue converges to four significant figures and the relative difference compared to $P = 8$ has dropped to approximately 0.002% at $P = 6$. In all the following computations involving both NS and LNS equations, $P = 6$ was adopted.

IV. BASE FLOWS

Base flows $\boldsymbol{U}$ were obtained by solving the NS equations (1) in a semi-domain with symmetry boundary conditions implemented on the x-axis, until the solution converged to a steady state. We then projected the velocity field from the half domain to the full domain, as illustrated in Fig. 2, for subsequent analysis based on the LNS equations (3). We note that since the unsteady NS equations are used to find the base flow in a semi-domain, the fact that steady solutions are obtained indicates that the base flows must be stable to symmetric disturbances over the range of Reynolds numbers employed.

As illustrated in Figs. 2(a)–2(c), contour lines of spanwise vorticity at level ± 0.01 are plotted to identify the border of the wake. We see in Fig. 2 that at $Re = 50$, the width of the wake expands downstream of the bubble, at $Re = 175$, the width is almost constant, while at $Re = 300$, the width contracts after passing the bubble. In Fig. 2(d) we define the bubble length L (measured from the centre of the square to the end of the bubble), the maximum width of the bubble W, and the

TABLE I. Convergence of the largest growth rate of perturbations, denoted as $\mathrm{Re}(\sigma_{\max})$, with respect to the polynomial order P used in each spectral element for flow past a square cylinder at $Re = 300$.

P	$\mathrm{Re}(\sigma_{\max})$	Relative difference
3	5.0883×10^{-2}	6.6×10^{-2}
4	4.8226×10^{-2}	1.1×10^{-2}
5	4.7822×10^{-2}	2.3×10^{-3}
6	4.7711×10^{-2}	2.0×10^{-5}
7	4.7710×10^{-2}	0
8	4.7710×10^{-2}	...

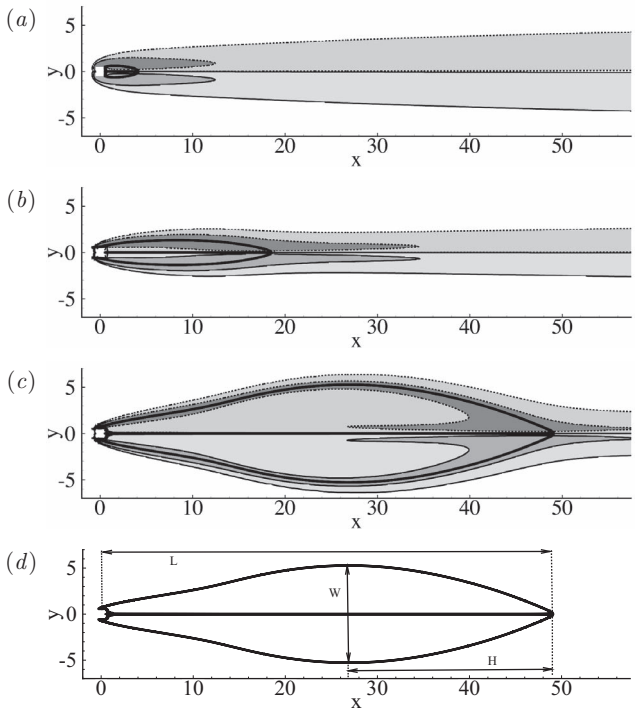

FIG. 2. Steady base flow passing a square cylinder at (a), $Re = 50$; (b), $Re = 175$; (c), $Re = 300$. Parameters related with the recirculation bubble are defined in (d). Thin solid lines are contour lines for vorticity 0.01 and 0.4 and thin dashed lines are contour lines for vorticity -0.01 and -0.4. The thick solid lines represent the border streamlines of the recirculation bubble.

downstream length H (measured from the widest point to the end of the bubble). It is seen that the ratio H/W is a measure of the "closing angle" of the bubble. Since the border of the bubble consists of streamlines, the larger H/W, the more parallel flow is downstream of the bubble.

Figure 3 compares the size of the recirculation bubble in flow past a square cylinder with that past a circular cylinder (in the latter case, the reference length d is the diameter of the cylinder—this was a separate set of calculations carried out for purposes of comparison). We see that the current calculations for a circular cylinder agree well with a previous investigation.[10] It is noted that over the range of Reynolds numbers considered, the bubble length is almost a linear function with respect to the Reynolds number in flow past a circular cylinder and for the square cylinder at lower Reynolds numbers, but increases rather more sharply at higher Reynolds numbers in flow past a square cylinder. This apparent discrepancy in behaviour is a consequence of the upper limit of Reynolds number, since it is found that for a circular cylinder, similar behaviour is observed, but at still larger Reynolds numbers.[10]

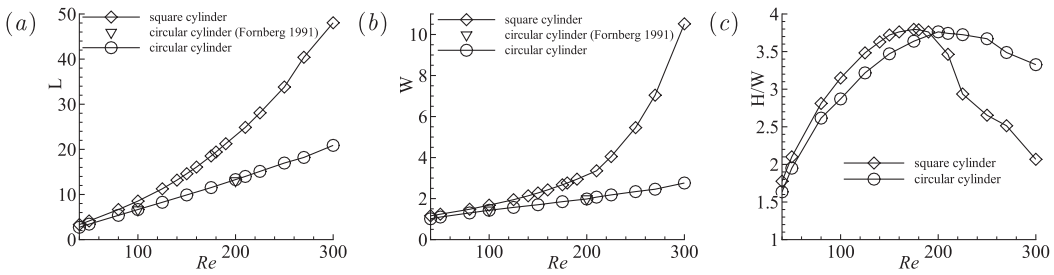

FIG. 3. Key parameters of base flow wakes for $40 \leq Re \leq 300$. (a), bubble length; (b), bubble width; (c), ratio of bubble closure length to width (see also Fig. 2(d)).

At $Re = 300$, the recirculation bubble downstream of a square cylinder is more than twice longer than the bubble downstream of a circular cylinder, indicating that the stability study for flow past a square cylinder requires more resolution and would be more sensitive to spatial discretization than the circular cylinder flow.

Bubble width exhibits similar trends as the length at increasing Reynolds number. As can be observed in Fig. 3(b), the bubble width for the circular cylinder flow increases almost linearly with the Reynolds number over the range considered while that for square cylinder expands much more rapidly for higher Reynolds number, after an almost linear initial increase. Similar behaviour was noted for flows past a circular cylinder by Fornberg, but the Reynolds number at which the steepening occurs for a circular cylinder is above the range we have considered.[10]

At $Re = 300$, the bubble for flow past a square cylinder is approximately four times wider than that in the circular cylinder flow. For Reynolds number higher than 300, owing to the rapid extension of the bubble, the current resolution does not yield well-converged results. Since the "closing angle" of the bubble is closely related with instabilities as will be discussed in Secs. V and VI, we present the ratio H/W, which quantifies this angle, in Fig. 3(d). It is observed that this ratio reaches maximum at $Re \approx 175$ in the square cylinder flow and $Re \approx 200$ in the circular cylinder flow, corresponding to the Reynolds numbers where flow downstream of the bubble is most parallel with the free stream velocity.

In general, the separation bubbles for symmetrical and laminar circular and square cylinder wakes display many similarities although the trends are generally characterised by lower Reynolds numbers in the case of the square cylinder. This is not very surprising given that for the square cylinder the separation points are fixed and the initial departure angle of the separation streamline must be 90°, so the wake is always liable to be wider than is the case for a circular cylinder at the same Reynolds number. This suggests that many of the stability outcomes to be described below for the symmetric wake of a square cylinder could be generalised to a circular cylinder wake, or indeed that of any symmetric two-dimensional bluff body.

V. GLOBAL STABILITY MODES

The growth rate of the most unstable mode for square cylinder flow is compared against those for circular cylinder flow in the range $40 \leq Re \leq 300$ in Fig. 4(a). It is seen that for the square cylinder case, the critical Reynolds number, above which the growth rate becomes positive, is $Re_c = 45$. This critical Reynolds number has also been calculated using the Stuart–Landau equation[11] as $Re_c = 45$ and measured in experiment[12] as $Re_c = 47 \pm 2$; both results agree very well with our prediction.

We see that for the square cylinder flow, the growth rate reaches maximum near $Re = 175$, while for circular cylinder flow, this "optimal" Reynolds number is approximately $Re = 200$, but for

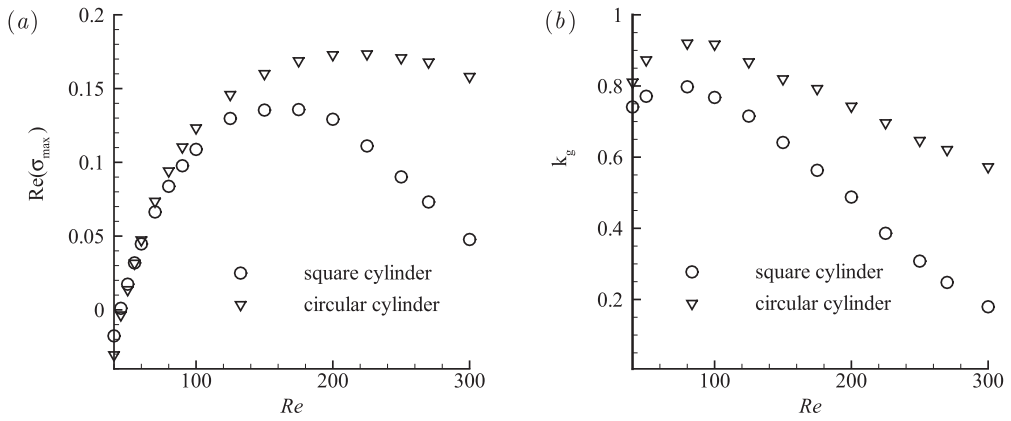

FIG. 4. Comparison of the instabilities for flow around a square cylinder and flow past a circular cylinder at $40 \leq Re \leq 300$. (a) Growth rate, i.e., $\mathrm{Re}(\sigma_{\max})$ and (b) dominant streamwise wavenumber of the global most unstable mode, denoted as k_g.

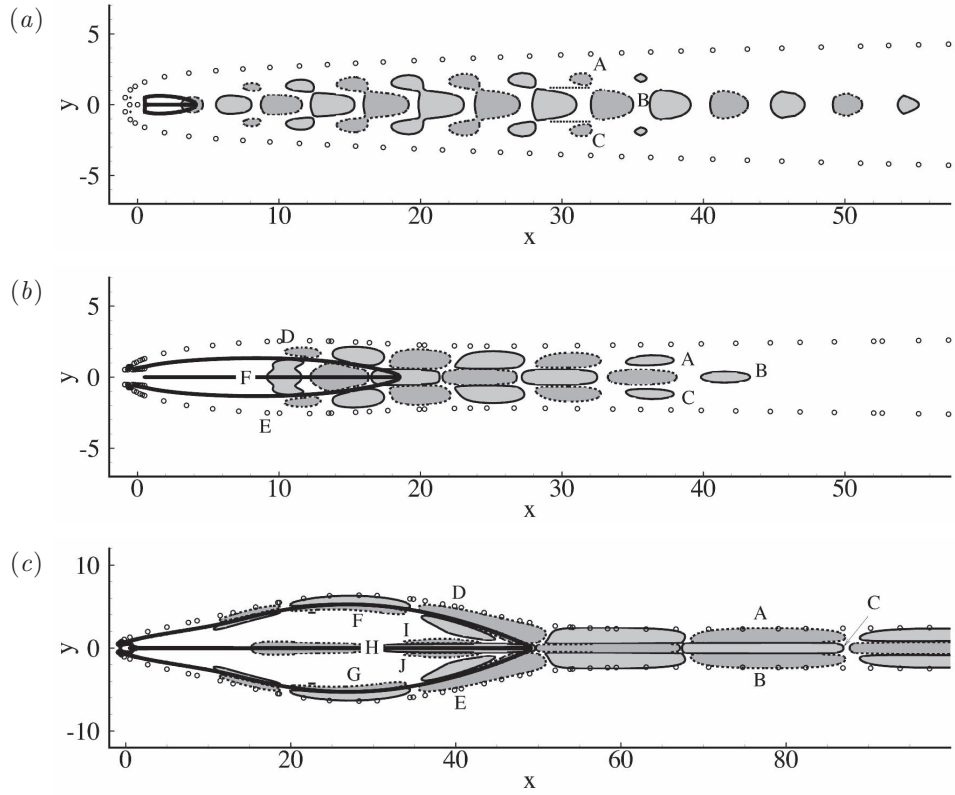

FIG. 5. Contours of vorticity for eigenmodes at (a), $Re = 50$; (b), $Re = 175$; (c), $Re = 300$. The contour levels are chosen to highlight structural information. Solid and dashed lines denote positive and negative contour levels, respectively. Hollow circles represent the border of the base flow wake (contour lines of base flow vorticity ± 0.01) and the thick solid lines are border streamlines of the recirculation bubble in the base flow as plotted in Fig. 2. In (a), the short dotted lines denote the positions of inflection points near $x = 30$.

larger Reynolds number, the growth rate for square cylinder flow drops more rapidly with Reynolds number than for the circular cylinder flow. We notice that the instability reaches maximum at almost the same Reynolds number as the ratio H/W, as shown in Fig. 3(c) for both circular cylinder flow and square cylinder flow. At these "optimal" Reynolds numbers, the border of the wake is almost parallel with the x axis, while for smaller and larger Reynolds numbers the border downstream of the separation bubble, respectively, expands and contracts. These observations suggest a conclusion that the flow becomes most unstable when the bubble instability and downstream shear flow instability are smoothly coupled.

Figure 4(b) shows the dominant, or most energetic streamwise wavenumber of the most unstable mode, obtained by Fourier decomposition of the streamwise velocity of the mode along the axis of the cylinder. We observe that at larger Reynolds numbers, when the separation bubble becomes longer, the wavenumber of the eigenmode decreases, and in the square cylinder flow, this dominant wavenumber decreases more rapidly with increasing Reynolds number than for the circular cylinder flow, owing to the more rapid extension of the bubble.

Structures of the most unstable eigenmodes are presented in Fig. 5. We see that at low Reynolds numbers, e.g., $Re = 50$, the structure of the eigenmode is associated with the wake downstream of the bubble (see Fig. 5(a)). This distribution agrees with previous experimental observations of the stability bifurcation in a circular cylinder flow: wake instability is associated with the formation of sinuous waves travelling downstream on the sides of the recirculation region.[13] In this locally unstable region, the distribution of the streamwise velocity in the y direction has two inflection points, whose vertical locations at $x = 30$ are marked by dotted lines. These inflection points induce inflection point instabilities. It is noted that on traverses in the y direction, the vorticity of the

eigenmode changes sign from "A" to "B," corresponding to crossing the inflection point above the axis and from "B" to "C," corresponding to crossing the inflection point below the axis.

At larger Reynolds number, e.g., $Re = 175$, the instability associated with the bubble becomes dominant and it is noticed that the instability extends upstream to the bubble owing to the inflection points on the upper and lower sides of the bubble (see Fig. 5(b)). We see that the sign of modal vorticity changes on traverses from "D" to "F," and from "F" to "E," which are associated with the inflection points on the upper and lower sides of the bubble. The positions of these inflection points are not marked in the figure since they are close to the border of the bubble, as discussed in the context of a recirculation bubble in a backward-facing step flow.[14]

When the Reynolds number is increased to $Re = 300$, the bubble expands extensively and the inflection point instabilities on both sides of the bubble become clearer. In Fig. 5(c), we see that vorticity strips "D" and "F" stem from the inflection points on the upper side of the bubble while "G" and "E" are associated with the lower inflection points. Inspecting magnitudes of the vorticity strips, we see that "D" and "E" are much stronger than "F" and "G" and therefore "D" and "E" induce another string of vorticity strips along the axis, marked as "H." Since "F" and "H" have the same signs and are spatially separated, they induce vorticity strips between them, marked as "I" and similarly "H" and "G" induce "J." We notice that at $Re = 175$, where the bubble is not large enough to accommodate these vorticity strips, the three strings of vorticity strips in the bubble observed in Fig. 5(c) ("F," "G," and "H") merge into a single string which was marked as "F" in Fig. 5(b), and therefore the induced vorticity strips "I" and "J" do not appear.

Also presented in Fig. 5 is the border of the wake, represented by contour lines of spanwise vorticity ± 0.01. We see that this border acts as an envelope of the eigenmode. As discussed above, at $Re = 50$, this envelope expands in the vertical direction downstream of the bubble, contracts at $Re = 300$, and is almost parallel with the axis of the square cylinder at $Re = 175$. The shape of this envelope indicates that the unstable structure associated with the bubble instabilities can be convected smoothly into the region downstream of the bubble at $Re = 175$, where the growth rate maximises.

VI. LOCAL STABILITY ANALYSIS

To better illustrate the mechanism that the growth rate reaches maximum when the base wake flow becomes parallel around the end of the bubble, we conduct local stability analyses based on the streamwise velocity component of the base flow by assuming that the base flow is locally parallel at each streamwise location. Growth rate of local eigenmodes with streamwise wavenumber k is shown in Fig. 6. The location of the end of the bubble is illustrated by dashed lines. The filled circles denote the points whose streamwise wavenumber and local growth rate agree with the dominant streamwise wavenumber (marked as k_g in Fig. 4(b)) and growth rate of the global mode (see Fig. 4(a)). Therefore the global stability characters can be largely represented by the local stability of the flow at the streamwise location of the circles.

It is seen that the maximum growth appears immediately downstream of the square and reduces for increasing x, while the most amplified streamwise wavenumbers are in the range $0.5 < k < 1$ over the parameters considered. However the contour lines are dense for the region close to the square, indicating that the stability characteristics of the base flow changes rapidly and that the base flow is not parallel, which breaks the assumption of the local stability analysis. Therefore the high local instabilities in the region around the square are not directly related to the global instabilities.

At $Re = 50$, it is seen from Fig. 6(a) that the cycle is located far downstream of the end of the bubble and at a frequency close to the locally most unstable frequency. This is because the wake far downstream of the bubble is more parallel and supports the global instabilities, while the locally most unstable region, which is upstream of the end of the bubble, does not support the global instabilities since the streamlines are unparallel (Fig. 2(a)) and show dramatic changes of the local growth rate.

As the Reynolds number increases to $Re = 175$, it is seen that the cycle moves towards the end of the bubble. This is because H/W increases with the Reynolds number (Fig. 3(d)) resulting in an increasingly parallel flow around the end of the bubble, which can support global instabilities and is locally more unstable than the downstream locations. Another point worth noting is that the

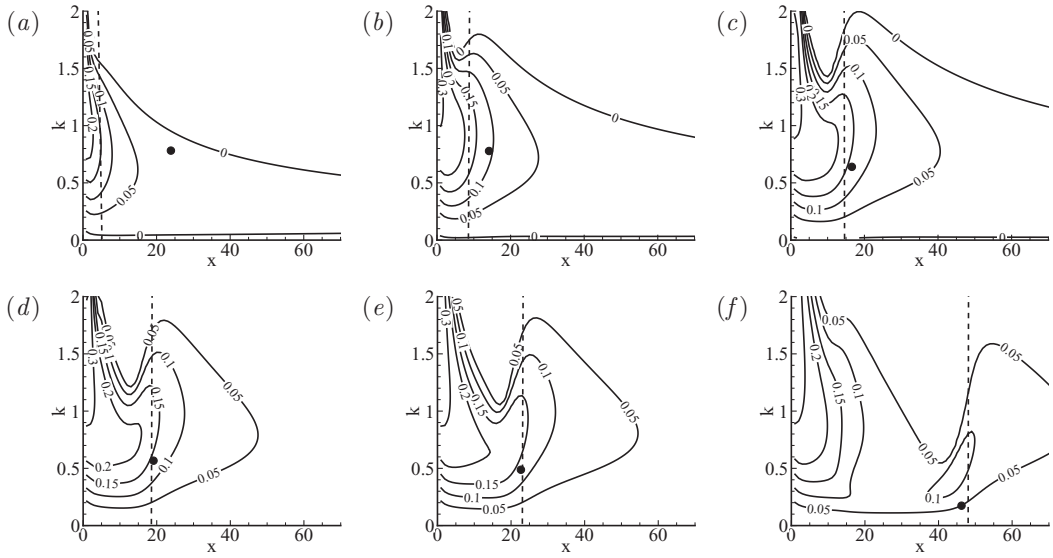

FIG. 6. Contours of growth rates from local stability analyses at (a) $Re = 50$, (b) $Re = 100$, (c) $Re = 150$, (d) $Re = 175$, (e) $Re = 200$, and (f) $Re = 300$. k denotes the streamwise wavenumber of local eigenmodes. The dashed lines represent the streamwise location of the end of the bubble as shown in Fig. 4(b). The filled circles have the local wavenumber and growth rate that agree with the wavenumber and growth rate of the global mode.

bubble induces a reduction of instabilities to high frequency perturbations and this reduction effect increases with the Reynolds number. In this range of the Reynolds number, this reduction effect has not affected the global mode yet, since the locally most unstable wavenumbers are $k < 1$ and the reduction effect only appears at $k > 1$.

As the Reynolds number increases beyond 175, the region upstream of the end of the bubble becomes more unparallel (Fig. 3(d)) and cannot support global instabilities. However the region downstream of the bubble is still parallel. Therefore the cycle does not move upstream further and is located around the end of the bubble. At $Re = 300$, the reduction effect of the bubble has penetrated into $k > 0.2$, resulting in dramatic change of amplifications of perturbations with $k > 0.2$. Therefore the local instabilities at $k > 0.2$, which relies on the parallel assumption, do not support global instabilities. As marked by the cycle, the global mode has a dominant frequency $k = 0.18$, which is locally smoothly amplified across the streamwise locations. It has been argued that in a circular cylinder flow, the instabilities develop from the end of the bubble,[2] which is consistent with this local study and the distribution of the global modes shown in Fig. 5.

All the local and global stabilities discussed above are based on the steady base flow. It is noticed that the wake of the mean flow of the nonlinear self-sustained oscillation state is not parallel and becomes shorter at higher Reynolds numbers.[15] Therefore it is expected that the distribution of eigenmodes is significantly different if the mean flow of the non-symmetric wake were to be adopted as the base flow. Even though it is observed that the most unstable eigenmode of the mean flow predicts the Strouhal number better than the symmetric base flow directly obtained from DNS, using mean flow as base flow has its own disadvantages. For example, the mean flow is a statistical construction and not a solution of the steady NS equations, and as revealed in the flow past a circular cylinder, the mean flow is marginally stable, which makes the stability analysis equivalent to a mode decomposition. In this work we focus on the bifurcation process, which is related with the development of perturbations on the basis of an unperturbed solution of the NS equations, and therefore we study the unperturbed symmetric base flow rather than the mean flow.

VII. CONCLUSION

The global stability of symmetrised flow around a square cylinder is studied at Reynolds numbers $Re \leq 300$ and compared to circular cylinder flow. The base flow is obtained by DNS on

a semi-domain with symmetry boundary conditions on the axis of the cylinder and then projecting the converged steady flow field from the half domain to the full domain. The fact that steady base flows are obtained using DNS in the semi-domain shows that the base flows are stable to symmetric disturbances, in agreement with the linear stability analysis. It is observed that the length and width of the recirculation bubble downstream of the square cylinder increases with Reynolds number over the range of values considered in a manner consistent with that for the symmetric wake (albeit at higher Reynolds numbers) of a circular cylinder.[10]

The critical Reynolds number, i.e., the threshold for asymptotic instability is observed to be $Re_c = 45$, which agrees well with the published results.[11,12] At Reynolds numbers above the critical value, three typical unstable eigenmodes are identified. At Reynolds number slightly higher than Re_c, e.g., $Re = 50$, the most unstable eigenmode is associated with the inflection points in the wake downstream of the bubble. At increasing Reynolds number, the inflection points around the upper and lower sides of the bubble induce instabilities, with the result that the unstable eigenmodes extend upstream into the bubble. At $Re > 175$, when the bubble significantly expands, induced vorticity strips are observed along the axis inside the bubble and the growth rate of the eigenmodes reduces at further increasing Reynolds numbers. Inspecting the border of the wake in the base flow, we see that the most unstable base flow corresponds to a parallel wake border and a minimum closing angle of the bubble.

Using local stability analyses, it is shown that the region around the cylinder is locally most unstable but the stability characteristics change rapidly in the streamwise direction and cannot support global instabilities. As Reynolds number increases, the bubble induces a reduction of local instabilities to high frequency perturbations, which also results in significant change of stabilities over the streamwise direction and fails to support global modes with high frequency. For $Re < 175$, the streamwise location which determines the global stabilities moves towards the end of the bubble and the dominant wavenumber does not change dramatically; for $Re > 175$ the point is always associated with the end of the bubble, but the wavenumber of the global modes reduces owing to the reduction effect associated with the expanding bubble.

The three-dimensional development of the vortex shedding state at $Re > 190$ (for circular cylinder flow) was not considered in the scope of the current work. It is worth noticing that all the global modes calculated in this work are anti-symmetric with respect to the axis of the cylinder. However, symmetric unstable modes could appear if the shear layer became unstable to two-dimensional Kelvin–Helmholtz instabilities at $Re > 1000$,[6] which is much larger than that considered in this work.

ACKNOWLEDGMENTS

We are grateful for financial support from the Australian Research Council through Discovery Program Grant No. DP1094851, and from Australia's National Computational Infrastructure via Merit Allocation Scheme Grant No. D77.

[1] A. Roshko, "Perspectives on bluff body aerodynamics," J. Wind Eng. Ind. Aerodyn. **49**, 79–100 (1993).
[2] C. H. K. Williamson, "Vortex dynamics in the cylinder wake," Annu. Rev. Fluid Mech. **28**, 477–539 (1996).
[3] D. Barkley and R. D. Henderson, "Three-dimensional Floquet stability analysis of the wake of a circular cylinder," J. Fluid Mech. **322**, 215–241 (1996).
[4] F. Marques, J. M. Lopez, and H. M. Blackburn, "Bifurcations in systems with Z_2 spatio-temporal and $O(2)$ spatial symmetry," Physica D **189**, 247–276 (2004).
[5] H. M. Blackburn, F. Marques, and J. M. Lopez, "Symmetry breaking of two-dimensional time-periodic wakes," J. Fluid Mech. **522**, 395–411 (2005).
[6] M. Braza, P. Chassaing, and H. Minh, "Numerical study and analysis of the pressure and velocity fields in the near wake of a circular cylinder," J. Fluid Mech. **165**, 79–130 (1986).
[7] D. Barkley, H. M. Blackburn, and S. J. Sherwin, "Direct optimal growth analysis for timesteppers," Int. J. Numer. Methods Fluids **57**, 1435–1458 (2008).
[8] J. A. C. Weideman and S. C. Reddy, "A MATLAB differentiation matrix suite," ACM Trans. Math. Software **26**, 465–519 (2000).
[9] H. M. Blackburn and S. J. Sherwin, "Formulation of a Galerkin spectral element–Fourier method for three-dimensional incompressible flows in cylindrical geometries," J. Comput. Phys. **197**, 759–778 (2004).

[10] B. Fornberg, "Steady viscous flow past a circular cylinder up to Reynolds number 600," J. Comput. Phys. **61**, 297–320 (1985).
[11] D.-H. Yoon, K.-S. Yang, and C.-B. Choi, "Flow past a square cylinder with an angle of incidence," Phys. Fluids **22**, 043603 (2010).
[12] A. Sohankar, C. Norberg, and L. Davidson, "Low-Reynolds-number flow around a square cylinder at incidence: Study of blockage, onset of vortex shedding and outlet boundary condition," Int. J. Numer Methods Fluids **26**, 39–56 (1998).
[13] J. Gerrard, "The wakes of cylindrical bluff bodies at low Reynolds number," Philos Trans. R. Soc. London, Ser. A **288**, 351–382 (1978).
[14] O. Marquet, D. Sipp, J. M. Chomaz, and L. Jacquin, "Amplifier and resonator dynamics of a low-Reynolds-number recirculation bubble in a global framework," J. Fluid Mech. **605**, 429–443 (2008).
[15] D. Barkley, "Linear analysis of the cylinder wake mean flow," Europhys. Lett. **75**, 750–756 (2006).